Full length article

Nanoscale compositional segregation and suppression of polar coupling in a relaxor ferroelectric

Teresa Roncal-Herrero [a], John Harrington [a], Aurang Zeb [b], Steven J. Milne [a, *], Andy P. Brown [a]

[a] School of Chemical and Process Engineering, University of Leeds, Leeds LS29JT, United Kingdom
[b] Department of Physics, Islamia College, Peshawar, KP, Pakistan

ARTICLE INFO

ABSTRACT

A number of relaxor ferroelectric ceramics have been demonstrated to possess a near stable value of relative permittivity over very wide temperature ranges. This cannot be explained by conventional theories of relaxors. One such system is based on the perovskite solid solution series: $(1-x)$ $(Ba_{0.8}Ca_{0.2})TiO_3$-$xBi(Mg_{0.5}Ti_{0.5})O_3$, giving stable relative permittivity from 150 to 500 °C. We show by scanning transmission electron microscopy and electron energy loss spectroscopic elemental mapping that nanoscale compositional segregation occurs in the temperature stable relaxor composition ($x = 0.55$), with Ba/Ti clusters some 2—4 nm in extent, separated by Bi-rich regions of comparable size. This nanomosaic structure is consistent with phase separation into a ferroelectrically active $BaTiO_3$ — type phase (Ba/Ti rich) and a weakly polar Bi/(Mg) rich perovskite solid solution. The possibility that nano-phase segregation is the cause of weak dipole coupling and suppression of the dielectric relaxation peak is considered.

1. Introduction

There is a growing requirement to develop new capacitor materials that can operate reliably at temperatures >200 °C for use in electronic systems in harsh environments, for example engine control and management systems in the aerospace and automotive sectors, and for power electronics in the renewables sector. Commercial high-relative permittivity dielectrics are based on ferroelectric $BaTiO_3$. Microscale chemical segregation induced by chemical doping creates a core shell grain structure which smears out the Curie peak. This approach has provided the basis for the present generation of high-temperature commercial Class II capacitors that exhibit stable capacitance C_{25C} ±15% from a lower operating temperature of −55 °C to an upper limit of 125 °C in materials designated X7R by the Electronics Industries Alliance. Other modifications create slightly higher upper specified temperatures of 150 °C (X8R) and 175 °C (X9R).

In response to demands for Class II capacitors that can operate at ≥ 250 °C, a range of ceramic solid solutions have been reported in recent years for which stable relative permittivity, ε_r (±15%), is displayed over wide ranges of temperature, with ceiling temperatures of 300 °C—500 °C, far exceeding the operating limit of commercial Class II capacitors. Examples include the following solid solutions with substitution on A and B sites of the $BaTiO_3$ perovskite lattice; $BaTiO_3$-$BiScO_3$, $BaTiO_3$-$Bi(Mg_{0.5}Ti_{0.5})O_3$, $BaTiO_3$-$Bi(Zn_{0.5}Ti_{0.5})O_3$, and $(Ba_{0.8}Ca_{0.2})TiO_3$-$Bi(Mg_{0.5}Ti_{0.5})O_3$ [1—5]. These systems can show a progression of dielectric properties from ferroelectric to diffuse ferroelectric through to a normal relaxor ferroelectric with broad frequency-dependent dielectric peak (at T_m) at low to moderate levels of substitution.

Cation displacements in the ABO_3 unit cell result in unit cell dipoles in both a classic ferroelectric and a relaxor ferroelectric but the length scales of coherence of dipole coupling through the lattices differ: microscale in ferroelectrics and nanoscale in relaxor ferroelectrics. At high levels of compositional complexity, close to the solid solution limit (identified by X-ray diffraction) in the examples cited here, a strong relaxor peak in ε_r-T plots is replaced by a gently rising plateau giving ±15% stability in ε_r to upper limits from 300 °C to 500 °C [1—6]. The changeover from normal relaxor to temperature stable ε_r-T response in the

$(Ba_{0.8}Ca_{0.2})TiO_3$-$Bi(Mg_{0.5}Ti_{0.5})O_3$ system, with assumed Bi^{3+} and Ca^{2+} substitutions on Ba^{2+} sites, and Mg^{2+} on Ti^{4+} sites [4] is shown in Fig. 1: Mg and Ca split site occupancy may also occur [7,8].

Most theories to account for the dielectric response of a normal relaxor, for example the widely studied $Pb(Mg_{1/3}Nb_{2/3})O_3$-$PbTiO_3$, consider that as the sample cools from the high temperature paraelectric phase, polar nanoclusters or nanoregions form at the so called Burns temperature, T_B [9–16]. The size and coupling of these nanodomian regions increases on further cooling but reorientation dynamics become more sluggish: this together with a range of relaxation times results in a broad, frequency dependent peak at T_m in ε_r-T plots. Ultimately the nanodipole structures 'freeze' as the material changes from the ergodic to non-ergodic regime. Compositional heterogeneity involving charge and size mismatches on the host perovskite lattice is considered to create fluctuating electrostatic and stress fields that prevent the long-range dipole coupling and polar alignment of a classic ferroelectric [9–13]. The presence of B-site cations which are ferroelectrically inactive or less active than Ti can also act to inhibit long range dipole coupling.

In an attempt to gain some understanding of mechanisms that suppress the relaxation peak, a combination of high resolution X-ray and neutron diffraction, neutron total and electron diffuse scattering have been used by others to investigate $BaTiO_3$-$BiScO_3$ and $BaTiO_3$-$Bi(Zn_{0.5}Ti_{0.5})O_3$ with the aid of Reverse Monte Carlo simulations [17–19]. These studies have confirmed cation displacement directions, possible correlations of Bi and Ti displacements, and local tetragonal distortions over a few unit cell length scales in a globally cubic structure. However mechanistic links between dielectric properties and cation distributions on the nano and sub-nano scale remain elusive.

This paper reports the results of scanning transmission electron microscopy (STEM) analysis using both energy dispersive and electron energy loss spectrometries to probe the chemical composition of (1-x) $(Ba_{0.8}Ca_{0.2})TiO_3$-$xBi(Mg_{0.5}Ti_{0.5})O_3$, at a variety of length scales for both a composition exhibiting normal relaxor characteristics (x = 0.1, Fig. 1a) and a temperature-stable composition with a severely suppressed dielectric peak (x = 0.55, Fig. 1b). Direct imaging of nano-chemistry by STEM is potentially an important tool in the quest to understand the atomistic reasons for the suppression of a normal relaxor ε_r peak. Scanning electron microscopy does not show any clear chemical or microstructural non-uniformity at the micro or submicrometer scales in either sample [6]. In the present work, distinctive nanomosaic chemical segregation has been discovered in the temperature stable relaxor which together with lattice defects inferred by composition analysis offers a potential explanation for the suppression of the normal thermal evolution of polarization in the ergodic regime of a relaxor.
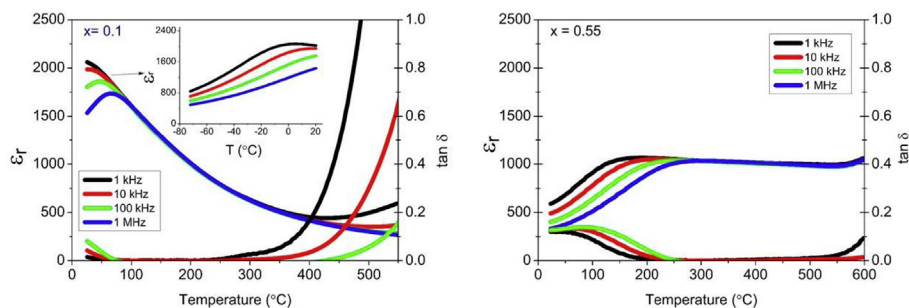
2. Experimental section

Ceramics of (1-x) $(Ba_{0.8}Ca_{0.2})TiO_3$-$xBi(Mg_{0.5}Ti_{0.5})O_3$ were produced following the method described in detail in Refs. [4,6]. As a general summary, appropriate quantities of the starting powders were weighed to meet the target compositions and processed by a conventional mixed oxide route. The dried, mixed powders were calcined at 850 °C for 4–6 h and pressed into pellets by uniaxial pressing at 150 MPa. Sintering was carried out in air in closed alumina crucibles at 1050 °C for 4 h; powder compacts were embedded in a calcined powder of the same composition to minimize volatilization loss. Two compositions were prepared, x = 0.1 of notional formula $Ba_{0.72}Ca_{0.18}Bi_{0.1}Mg_{0.05}Ti_{0.95}O_3$ and x = 0.55 of notional formula $Ba_{0.36}Ca_{0.09}Bi_{0.55}Mg_{0.275}Ti_{0.725}O_3$.

Samples were prepared for electron microscopy by crushing the pellets using an agate mortar until a fine powder was obtained. The fine powder was then dispersed in ethanol and sonicated for at least 3 min in an ultrasonic bath. Suspensions were dropcast onto holey carbon film supported on 400 mesh copper grids (*EM* resolutions Ltd). An alternative method of sample preparation involved cutting a thin lamella using a Focused Ion Beam FEI Helios G4 CX Dual Beam microscope and in-situ-lift out onto dedicated support grids for TEM (Omniprobe Inc). Once mounted on the support grids, ion beam cleaning was undertaken at 5 kV and 41 pA beam currents to produce a lamella of 50 nm or lower nominal thickness (by SEM image) with minimal side-wall damage.

Thin samples were analyzed by a FEI Titan Themis[3] transmission electron microscope operated at 300 kV with a monochromator, a Super-X 4-detector silicon drift energy dispersive X-ray (EDX) system and a Gatan GIF Quantum 965 electron energy loss spectrometer (EELS). The monochromator provides continuous beam current control in STEM when not excited and the X-FEG source provides an energy spread of ~1.1 eV (FWHM of zero loss peak) in this condition. STEM is run with a 1.4 Å probe diameter of 10 mrad convergence semi angle; probe currents were varied by the monochromator and ranged from 40 to 200 pA depending on the imaging and mapping mode. High angle annular dark field (HAADF) images were collected over the scattering semi-angle range of 35–150 mrad. STEM-EEL spectra were collected with an 11 mrad collection semi-angle. EDX spectra were processed in Bruker Esprit Software and EEL spectra processed in Gatan Microscopy Suite version 3.3.1.

3. Results

High angle annular dark field (HAADF)-STEM imaging and corresponding elemental mapping by STEM-EDX of FIB-prepared lamellae from both the x = 0.1 and x = 0.55 samples show a micrometer grain structure, Fig. 2, as previously observed by SEM [4,6]. Bright contrast at grain boundaries in the HAADF-STEM

Fig. 1. Measured dielectric properties of (1-x) $(Ba_{0.8}Ca_{0.2})TiO_3$-$xBi(Mg_{0.5}Ti_{0.5})O_3$ for a) x = 0.1, a strongly coupled normal relaxor composition and b) x = 0.55 a weakly coupled, temperature stable relaxor composition (as previously reported in Zeb et al., 2015 [6]).
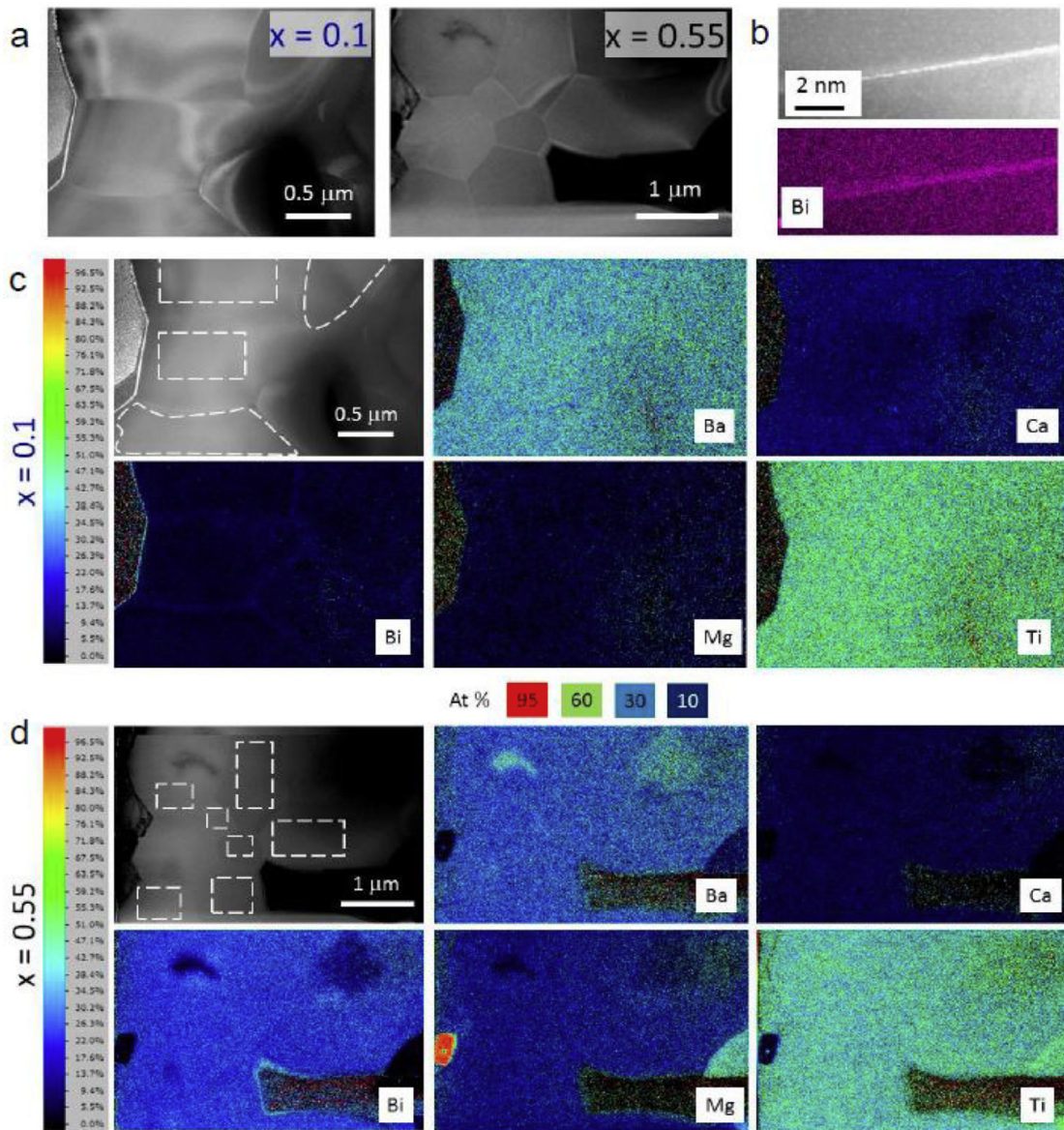
Fig. 2. HAADF STEM imaging and STEM-EDX elemental maps of FIB lamella cut from x = 0.1 and x = 0.55 BCT-BMT pellets. (a) HAADF STEM images (top left and middle reveal the grain structure and size (~1 μm), and indicate some heavy-element segregation at grain boundaries of both x = 0.1 and x = 0.55 materials. (b) Higher magnification HAADF STEM and elemental X-ray maps show Bi segregation to grain boundaries. (c) Elemental maps of x = 0.1. (d) Elemental maps of x = 0.55. The white boxes in the HAADF STEM images of c) and d) indicate regions of grains (not including grain boundaries) that were used for compositional assessment of EDX spectra (Table 1).

images suggest intergranular heavy-element segregation in both x = 0.1 and 0.55 (Fig. 2a). The EDX analysis confirmed a Bi-rich phase at grain boundaries (Fig. 2b). Elemental X-ray maps of the x = 0.55 sample, reveal some localized variability on the ~1 μm scale. In addition, discrete Mg-rich grains were observed in x = 0.55. These features are consistent with microregions of incomplete solid state reaction in both samples. No evidence of any weak reflections due to secondary phases was present in XRD patterns, indicating secondary microscale phases (e.g. crystalline Mg-rich grains) observed by STEM were present in only very minor quantities throughout the bulk ceramic [4,6].

Elemental quantities estimated by standardless, semi-quantitative analysis of EDX spectra, averaged over 4 and 7 grains for the x = 0.1 and x = 0.55 specimens respectively are presented in Table 1 (white doted areas in HAADF STEM images of Fig. 2). Since the titanium levels in the 'bulk' grains of the FIB lamella showed the

greatest spatial uniformity in the areas used for EDX analysis (Fig. 2) the counts for the other cations were normalized against the Ti content in the notional 'ABO₃' starting formula. The quantified areas excluded grain boundary phases or any other inhomogeneous regions. Oxygen content was not included in the analysis (because of sensitivity to absorption of the low energy O *K* X-rays due to specimen thickness and orientation). Cation vacancy levels were then estimated by subtracting the count for each of the other cations from the notional calculated ion fractions in a perovskite ABO_3 formula unit, and oxygen levels estimated by charge balancing against the total cation charge.

This approach suggests a deficit in the Bi, Ca and Mg levels for matrix grains in both x = 0.1 and 0.55. Table 1 indicates the relative differences in elemental contents of each sample ({difference in analyzed and notional values}/{notional value}). The Bi deficit is consistent with diffusion to grain boundaries and anticipated

Table 1
Measured (by STEM-EDX) and notional composition of the (a) x = 0.1 and (b) x = 0.55 BCT-BMT pellets. EDX data were averaged over 4 and 7 grains (not including grain boundaries or segregated features) for x = 0.1 and x = 0.55 BCT-BMT respectively, indicated by white boxes in Fig. 2. Atomic percentages obtained by STEM-EDX were normalized to nominal titanium levels to show the difference in other cation levels between the measured and notional compositions (from starting ratios of reagents).

	EDX STEM At % normalized to Ti = 0.95 x = 0.1 BCT-BMT	Notional At%	Average relative difference %		EDX STEM At % normalized to Ti = 0.725 x = 0.55 BCT-BMT	Notional At%	Average relative difference %
Ba	36.1 ± 5.7	36	0	**Ba**	18.5 ± 2.5	18	3
Ca	7.0 ± 0.1	9	−22	**Ca**	3.9 ± 0.1	4.5	−16
Bi	3.8 ± 0.9	5	−26	**Bi**	18.7 ± 3.9	27.5	−32
Mg	0.8 ± 0.1	2.5	−68	**Mg**	7.0 ± 0.2	13.8	−49
Ti	47.5 ± 2.8	47.5	0	**Ti**	36 ± 1.8	36.02	0

volatilization from the sample (despite the use of an atmosphere powder on sintering). The Mg and Ca are deficient within the matrix analyzed due to the spatial variability identified in EDX maps (enriched regions were excluded from the analysis, Fig. 2c and d). Due to the much lower Mg content in the x = 0.1 bulk sample, such grains were only detected by STEM-EDX in x = 0.55. Likewise the Bi rich grain boundary phase was more prevalent in x = 0.55. Based on these findings, the x = 0.55 ceramic would contain greater (absolute) levels of inferred cation and oxygen vacancies.

In terms of chemical formulae, the EDX derived cation ratios normalized to the expected Ti content per formula unit for the x = 0.1 matrix (0.95) corresponds to $Ba_{0.71}Ca_{0.14}Bi_{0.08}Mg_{0.02}Ti_{0.95}$ compared to the notional formula $Ba_{0.72}Ca_{0.18}Bi_{0.1}Mg_{0.05}Ti_{0.95}$ (based on ratios of starting reagents and expected composition; Table 1a). For the x = 0.55 specimen there was a more obvious deviation from the notional cation ratios per formula unit. The matrix grain composition is estimated at $Ba_{0.37}Ca_{0.08}Bi_{0.37}Mg_{0.14}Ti_{0.725}$ against a notional formula, $Ba_{0.36}Ca_{0.09}Bi_{0.55}Mg_{0.275}Ti_{0.725}$ (Table 1b). Taking charge balance and inferred

lattice vacancies (V) into account, the full chemical formula for the x = 0.55 matrix may be represented as $Ba_{0.36}Ca_{0.09}Bi_{0.55}Mg_{0.275}V_{Bi0.18}V_{Mg0.14}Ti_{0.725}O_{2.58}V_{O0.42}$.

Atom column resolution images of the perovskite lattice were obtained from relatively low current (40 pA) HAADF-STEM imaging of the x = 0.1 and x = 0.55 powders of crushed sintered pellets, drop-cast onto holey carbon films. Nanoscale (light) contrast variations over ≤ 5 nm length scales were apparent in each material (Fig. 3). HAADF-STEM imaging and X-ray elemental mapping (by STEM-EDX) reveal these light contrast regions to be dominated by Bi, (Fig. 4). They are mobile under higher current electron beam conditions (>80 pA) preventing detailed EDX analysis of the atom column resolution images, such as Fig. 3b and d, and they coalesced under prolonged electron irradiation (Fig. 4d) neither of which is resolved in the lower magnification imaging and mapping of the FIB sections (Fig. 2). The finding that these clusters are mobile and grow under prolonged irradiation could indicate they are produced by the irradiation (at very high vacuum) and/or by re-deposition on the matrix from grain boundary regions during TEM specimen
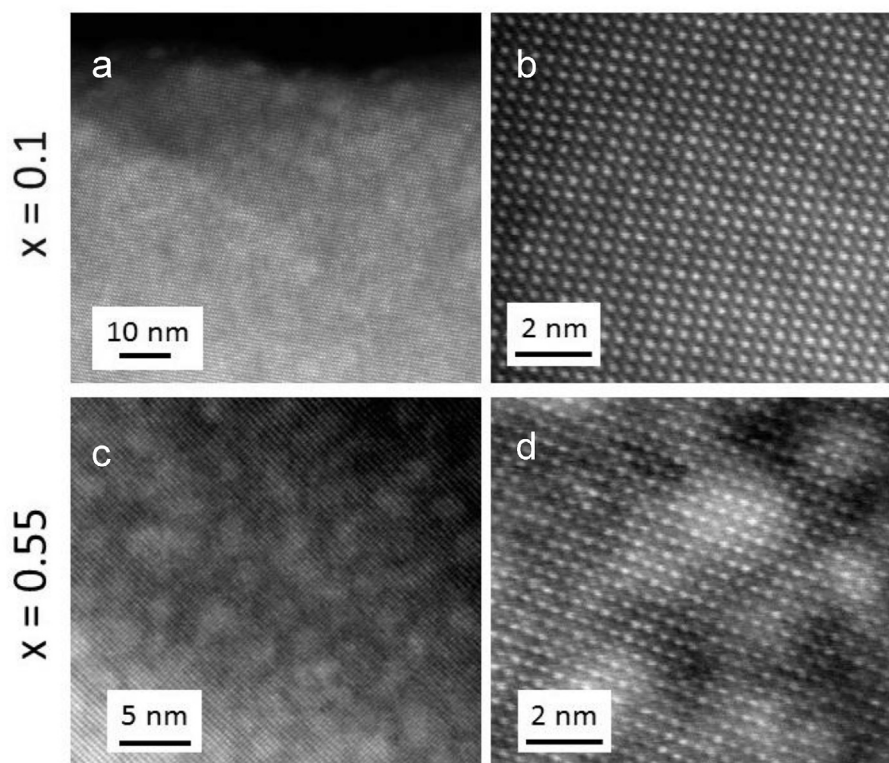

Fig. 3. Low current HAADF STEM imaging of crushed powders of sintered pellets reveals contrast variation consistent with compositional clustering in both the x = 0.1 (a−c) and x = 0.55 (b−d) lattices. The heavy element clusters are ~2 nm and present in both samples but more prevalent and visible in the higher Bi-content x = 0.55 sample.
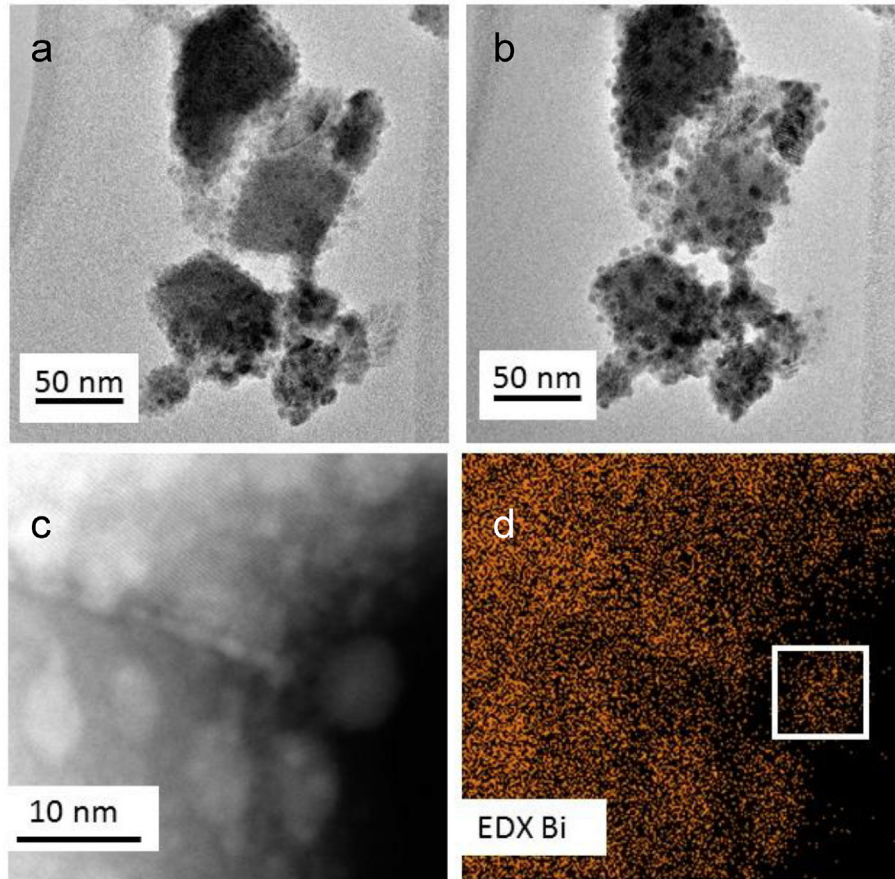
Fig. 4. Bright field TEM of x = 0.55 BCT-BMT of crushed powders (a) at low electron dose and (b) after prolonged electron irradiation. (c) Prolonged imaging by HAADF-STEM shows these clusters migrate to the edge of grains (d) STEM-EDX mapping with standard-less quantification of EDX spectra from a grain surface nanoparticle (indicated by box inset into Bi X-ray map) suggest they become Bi-metal after very prolonged irradiation (Bi = 89.6 ± 12.2 at.%, O = 8.2 ± 0.4 at.%, Ba = 3.3 ± 1.2 at.%).

preparation. Alternatively they may be an indirect consequence of bismuth oxide vaporisation during high temperature ceramic processing i.e. are a genuine feature of these ceramics.

Light contrast regions in HAADF-STEM images which we identify by EDX to be Bi-rich appear in other Bi containing ceramics with very different electrical properties to BCT-BMT. We have observed similar <5 nm clusters in cryo-STEM and low-kV SEM imaging of powders of the normal relaxor $(Na_{0.5}Bi_{0.5})TiO_3$ and the piezoelectric relaxor $(K_{0.5}Bi_{0.5})TiO_3$-$Bi(Mg_{0.5}Ti_{0.5})O_3$ (data not shown). Other groups report a similar observation for sodium bismuthate $(NaBiO_3)$ and in the Pb-free piezoelectric $Na_{0.5}Bi_{0.5}TiO_3$-$BaTiO_3$ [20,21].

Although elemental X-ray mapping of the atomic lattices by HAADF-STEM was unsuccessful because of the mobility of the Bi-rich areas under the prolonged irradiation required to generate sufficient signal to noise to reveal elemental segregation in these X-ray maps, these areas could be mapped by electron energy loss spectrum imaging, EELS (Fig. 5). Here a single dwell of 0.1 s per pixel was used to collect energy loss spectra over an 11 nm by 10 nm area of both the x = 0.1 lattice (0.4 nm pixel size) and the x = 0.55 lattice (0.2 nm pixel size).

The corresponding EELS maps resolve no specific elemental segregation for x = 0.1. However the x = 0.55 specimen shows compositional segregation, with Ba and Ti enrichment over length scales of approximately 2–5 nm. Intervening regions (of similar dimensions) show some evidence of Bi enrichment but not to the extent of the Bi rich areas identified by prolonged irradiation HAADF–STEM and EDX (Fig. 4 c and d). Levels of Mg and Ca were

too low to be detected by EELS. The Ba/Ti and Bi nano-segregation is further evident in spectra averaged over areas on and off a HAADF-image high-contrast cluster within the mapped area of the x = 0.55 specimen (black and red boxes and corresponding spectra inset in Fig. 5 respectively).

4. Discussion

By a combination of STEM HAADF imaging and EDX and EELS chemical analysis techniques, the above results disclose a range of chemical non-uniformities in each of the BCT-BMT materials under investigation. The central challenge to interpreting the features identified by our analysis lies in distinguishing spurious effects, for example incomplete solid state reactions, or mobile Bi clusters that are common to other Bi containing ceramics, from those which may be directly related to the suppression of the permittivity peak in the x = 0.55 ceramics.

Within any multicomponent ceramic prepared by conventional mixed oxide processing, there is a likelihood of localized chemical and/or phase variability because of kinetic limitations that prevent chemical equilibrium being achieved. This is particularly the case in materials which contain a mixture of refractory (e.g. MgO and TiO_2) and volatile (e.g. Bi_2O_3) starting components, especially if the sintering temperatures are close to the melting or partial melting temperature of the ceramic, as is the case here (sintering temperatures are only ~ 100 °C below partial melting temperatures).

Microstructural chemical inhomogeneities common to x = 0.1 and 0.55 can be discounted as playing any significant role in
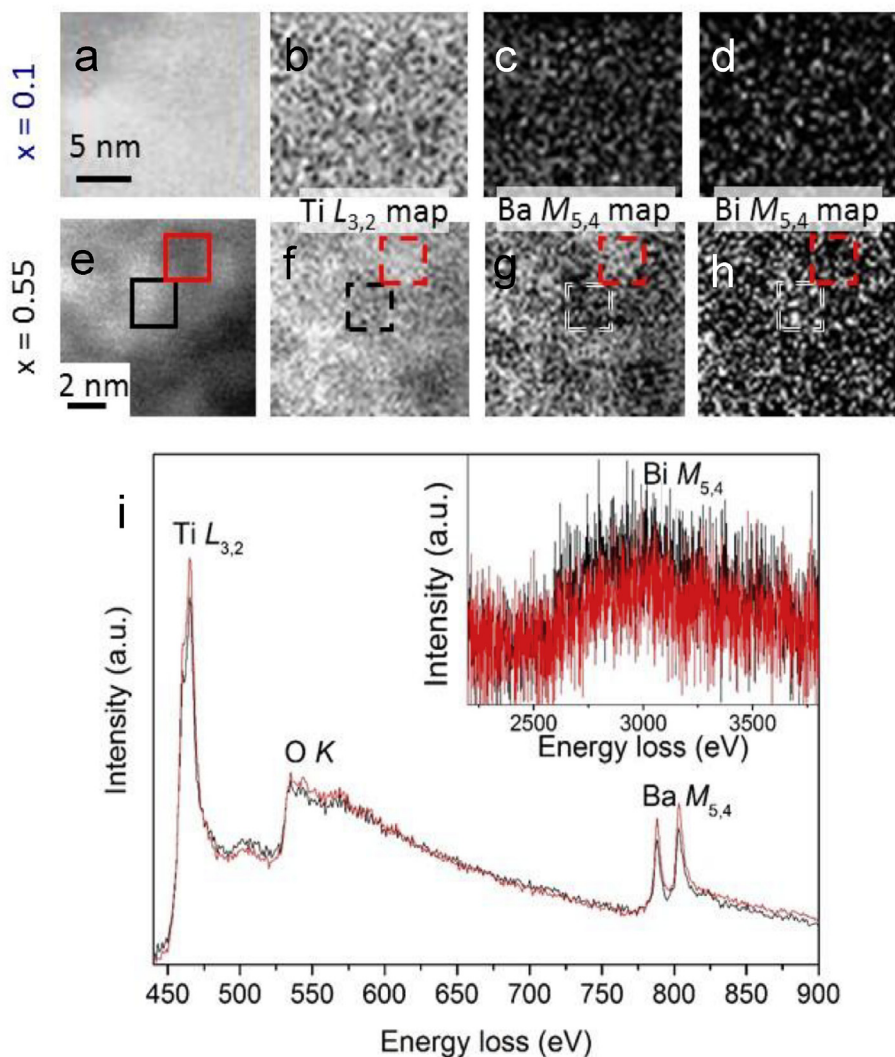
Fig. 5. EELS elemental mapping of crushed powders of sintered pellets. (a–d) x = 0.1: HAADF image (a) shows little or no compositional variation; (b) Ti $L_{3,2}$, (c) Ba $M_{5,4}$ and (d) Bi $M_{5,4}$ electron energy loss elemental maps show no detectable compositional variation. (e–h) x = 0.55: HAADF image (e) shows high contrast clusters indicating nanoscale compositional clustering in lattice; (f) Ti $L_{3,2}$, (g) Ba $M_{5,4}$ and (h) Bi $M_{5,4}$ electron energy loss elemental maps showing clear compositional clustering in x = 0.55. i) Background subtracted Ti $L_{3,2}$, O K and Ba $M_{5,4}$ and Bi $M_{5,4}$ energy loss edges extracted from the black and red boxes inset in (e) confirm the lattice regions of high contrast in the STEM HAADF image of x = 0.55 are Bi rich plus Ti and Ba deficient (black inset). (For interpretation of the references to colour in this figure legend, the reader is referred to the Web version of this article.)

suppressing the relaxation peak. This leads us to highlight the likelihood that the 2–5 nm nanomosaic structure identified by EELS in x = 0.55 (Fig. 5) is a significant factor in moderating the dielectric response and creating a temperature-stable relative permittivity over wide temperature ranges. The differences in chemical compositions required to generate contrast differences by EELS signals (such as those seen in Fig. 5) may typically be only a few atom %, but the analysis was performed through the full depth of crushed grains (which could be as thick as 50–70 nm). Therefore the actual enrichment in Ba and Ti within individual nanoregions may be much higher and the differences in chemical formulae between the two phases greater than indicated by 'averaged' data presented in Table 1.

As to why such a nanochemical segregation should occur, our previous ceramic scoping experiments indicate that the x = 0.55 composition coincides with the solid solution boundary detected by XRD (beyond which a bismuth titanate secondary phase forms) [4,6]. We interpret the identified nano-segregation as being indicative of incipient structural disruption of the lattice as it struggles

to accommodate high levels of Bi and Mg. The BMT theoretical end-member of the solid solution is thermodynamically unstable. There are reports it can be made at high pressure, but even then it is thermally unstable and decomposes to an anti-ferroelectric, orthorhombic phase [22]. The distinctive nanostructure of BCT-BMT x = 0.55, with Ba/Ti rich and Bi rich 2–5 nm compositional regions is consistent with the onset of thermodynamic instability and immiscibility.

Based on these interpretations, there are two aspects of the chemical nanostructure that would affect the dielectric properties of BCT-BMT and suppress the ε_r peak in x = 0.55; nano-chemical segregation and lattice vacancies. Each would inhibit the degree of order within polar nanodomains as they mitigate against coherent coupling of dipoles and re-orientation under an electric field. Chemical variability will also induce distinctive strain variations across the mosaic structure that will act against dipole growth.

Our proposition based on the new STEM-EELS evidence shown here is that the formation of the nanomosaic chemical structure
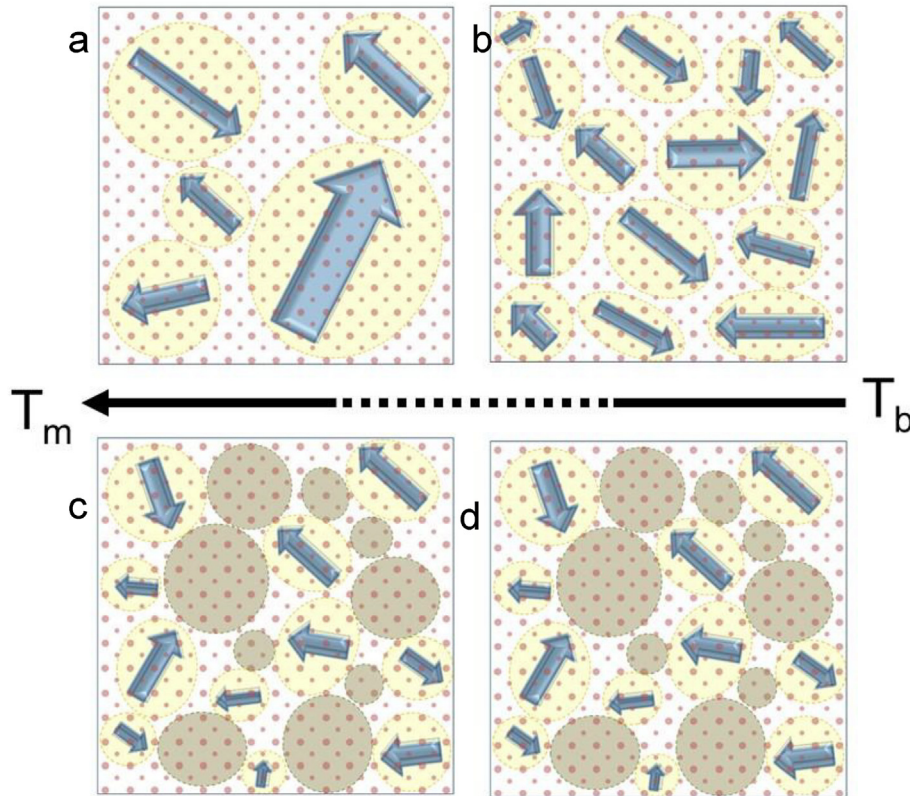
Fig. 6. Schematic of nanopolar structure of BCT-BMT lattices in the ergodic regime $T_m < T < T_b$ (T_b is the Burns temperature): (a, b) Normal relaxor with coherent crystal lattice and polar growth and alignment on cooling (blue arrows) [15]. (c, d) temperature stable relaxor with coherent lattice that has phasesegregated 2–5 nm nanopolar regions (light shading with blue arrows) which have restricted growth as temperature decreases due to co-existing weakly polar phase (dark shading). (For interpretation of the references to colour in this figure legend, the reader is referred to the Web version of this article.)

and the associated phase fragmentation controls re-ordering interactions between the ferroelectrically more active Ba/Ti rich, regions and the weakly polar Bi rich, Ba/Ti deficient regions. The latter are assumed to be richer in Mg (for reasons discussed below) although the Mg signal was too weak to detect. Thus, we tentatively designate these as Bi/Mg rich regions: Mg–containing unit cells being intrinsically less ferroelectrically active restrict length scales of polar order. Our premise is that as the sample cools toward Tm, the nanophase segregation and chemical non-coherence on the 2–5 nm length scales inhibits polar order beyond the spatial dimensions of the Ba/Ti rich regions.

These interpretations are represented in a schematic of the evolution of polar structure (Fig. 6) for: (a) a normal relaxor (x = 0.1) in which the multicomponent ions are distributed throughout a single-phase lattice; and (b) a phase-separated, nanomosaic structure which acts to confine polar order across the lattice and prevent the normal thermally induced evolution of polar structure, thereby creating a temperature-stable relaxor (x = 0.55). There is still a 'freezing' onset temperature (at $T < T_m$) but the size of domains varies little with temperature in the ergodic regime and a gently rising plateau is observed in ε_r-T plots. This discovery indicates that modelling of this type of material should not assume a homogeneous single-phase system.

Lattice vacancies inferred from EDX data (Table 1) also act against dipole coupling, due to electrostatic considerations. Despite significant inferred lattice vacancies from STEM-EDX, the current materials have low electrical conductivity, which can be explained by the formation of defect associates or clusters, e.g. VBi-VO, VMg-VO, MgTi-VO, which immobilize oxygen vacancies at low to moderate temperatures

[6,23].

Consideration of local electrical charge balance provides a framework as to understand why such a vacancy-rich, nanomosaic structure develops in BCT-BMT solid solutions. Local charge balance will create a preference for B-site Ti^{4+} ions to have Ba^{2+} or Ca^{2+} on neighbouring A-sites cations. Whereas for 'ABO$_3$' cells with B-site Mg^{2+} ions the expectation is for neighbouring A-site Bi^{3+} ions, but even so, this would not provide sufficient positive charge to balance three oxygen ions in an ABO$_3$ cell. Thus an oxygen vacancy mechanism is envisaged for local charge balance. The nominal solid solution formula of x = 0.55 has insufficient Ba and Ca ions to match the 0.725 Ti ions, thus a proportion of cells will include A-site Bi^{3+} where there is a B-site Ti^{4+}, and local electroneutrality points to Bi ion vacancies in such environments. Thus overall charge balance considerations lead to expulsion of bismuth oxide.

The experimental evidence from STEM-EELS (Fig. 5) of discrete nanoregions of differing Ba/Ti and Bi content (and inferred Mg content) is consistent with these site preferences from charge balance perspectives. The BCT-BMT perovskite lattice can accommodate Bi and Mg substitutions at low values of x but at limiting concentrations (x = 0.55), clustering into distinct nanoregions occurs.

Displacements of Bi and split site occupancies of some of the Ca and Mg components across the lattice add further nuances to local charge balance considerations. Nevertheless a direct link between charge disorder, local electrical neutrality, phase segregation and inhibition of polar order seems worthy of further consideration in other temperature-stable relaxor ferroelectrics.

5. Conclusion

We present evidence that the transition from a normal to a temperature stable relaxor material of general chemical composition $(1-x)$ $(Ba_{0.8}Ca_{0.2})TiO_3-xBi(Mg_{0.5}Ti_{0.5})O_3$ is characterized by nanoscale chemical phase segregation identified by scanning transmission electron microscopy and electron energy loss spectroscopy. The resolved chemical variability and phase separation at the ≤ 5 nm scale of the crystal lattice and consequent nanomosaic structure comprising ferroelectrically active Ba/Ti rich and weakly polar Bi (and Mg) rich phases is proposed to act against dipole coupling and counteract thermal evolution of polar coherence in the ergodic regime, thereby suppressing the dielectric peak.

Acknowledgements

References

[1] H. Ogihara, C.A. Randall, S. Trolier-McKinstry, Weakly coupled relaxor behavior of (1-x)BaTiO$_3$–xBiScO$_3$, J. Am. Ceram. Soc. 92 (2009) 110–118.

[2] Q. Zhang, Z. Li, F. Li, Z. Xu, Structural and dielectric properties of Bi (Mg$_{1/2}$Ti$_{1/2}$) O$_3$–BaTiO$_3$, J. Am. Ceram. Soc. 94 (2011) 4335–4339.

[3] C.C. Huang, D.P. Cann, X. Tan, N. Vittayakorn, Phase transitions and dielectric properties in BaTiO$_3$-Bi(Zn$_{0.5}$Ti$_{0.5}$)O$_3$ perovskite solid solutions, J. Appl. Phys. 102 (2008) 1–5, 044103.

[4] A. Zeb, S.J. Milne, Stability of high-temperature dielectric properties for (1−x) Ba0.8Ca0.2TiO3−xBi(Mg0.5Ti0.5)O3 ceramics, J. Am. Ceram. Soc. 96 (2013) 2887–2892.

[5] A. Zeb, S.J. Milne, High temperature dielectric ceramics: a review of temperature-stable high-permittivity perovskites, J. Mater. Sci. Mater. Electron. 26 (2015) 9243–9255.

[6] A. Zeb, Lead-free Dielectric and Piezoelectric Ceramics, Ph.D. Degree Thesis University of Leeds, 2015.

[7] Y. Ho Han, J.B. Appleby, D.M. Smyth, Calcium as an acceptor impurity in BaTi0$_3$, J. Am. Ceram. Soc. 70 (1987) 96–100.

[8] L. Suchow, Bismuth magnesium titanate an unusual new perovskite, J. Inorg. Nucl. Chem. 30 (1968) 87–95.

[9] G.A. Smolenskii, Physical phenomena in ferroelectrics with diffused phase transition, J. Phys. Soc. Jpn. 28 (1970) 26.

[10] W. Kleemann, F.J. Schäfer, D. Rytz, Diffuse ferroelectric phase transition and long-range order of dilute KTa$_{(1-x)}$Nb$_x$O$_3$, Phys. Rev. Lett. 54 (1985) 2038–2041.

[11] G. Burns, F.H. Dacol, Glassy polarization behavior in ferroelectric compounds Pb(Mg$_{13}$Nb$_{23}$)O$_3$ and Pb(Zn$_{13}$Nb$_{23}$)O$_3$, Solid State Commun. 48 (1983) 853–856.

[12] D. Viehland, J.F. Li, S.J. Jang, L.E. Cross, M. Wuttig, Deviation from Curie-Weiss behavior in relaxor ferroelectrics, Phys. Rev. B 46 (1992) 8003–8006.

[13] P.M. Gehring, S. E Park, G. Shirane, Soft phonon anomalies in the relaxor ferroelectric Pb(Zn$_{1/3}$Nb$_{2/3}$)$_{0.92}$Ti$_{0.08}$O$_3$, Phys. Rev. Lett. 84 (2000) 5216–5219.

[14] H. Takenaka, I. Grinberg, A.M. Rappe, Anisotropic local correlations and dynamics in a relaxor ferroelectric, Phys. Rev. Lett. 110 (2013) 1–5, 147602.

[15] M. Matsuura, K. Hirota, P.M. Gehring, Z.G. Ye, W. Chen, G. Shirane, Composition dependence of the diffuse scattering in the relaxor ferroelectric compound (1-x)Pb(Mg$_{1/3}$Nb$_{2/3}$)O$_3$-xPbTiO$_3$ (0$\leq$ x $\leq$0.40), Phys. Rev. B 74 (2006) 1–10, 144107.

[16] H. Takenaka, I. Grinberg, S. Liu, A.M. Rappe, Slush-like polar structures in single-crystal relaxors, Nature 546 (2017) 391–395.

[17] V. Krayzman, I. Levin, J.C. Woicik, F. Correlated, rattling-ion origins of dielectric properties in reentrant dipole glasses BaTiO$_3$-BiScO$_3$, Appl. Phys. Lett. 107 (2015) 192903.

[18] I. Levin, V. Krayzman, J.C. Woicik, F. Bridges, G.E. Sterbinsky, T.-M. Usher, J.-L. Jones, D. Torrejon, Local structure in BaTiO$_3$-BiScO$_3$ dipole glasses, Phys. Rev. B 93 (2016) 1–5, 104106.

[19] T.-M. Usher, T. Iamsasri, J.S. Forrester, N. Raengthon, N.M. Triamnak, D.P. Xann, J.L. Jones, Local and average structures of BaTiO$_3$-Bi(Zn$_{1/2}$Ti$_{1/2}$)O$_3$, J. Appl. Phys. 120 (2016) 1–13, 184102.

[20] S. Sepulveda-Guzman, N. Elizondo-Villarreal, D. Ferrer, A. Torres-Castro, X. Gao, J.P. Zhou, M. Jose-Yacaman, In situ formation of bismuth nanoparticles through electron-beam irradiation in a transmission electron microscope, Nanotechnology 18 (2007) 1–6, 335604.

[21] Z. Yingyi, TEM Study of Sodium Bismuth Titanate and Bismuth Nanoparticle Growth under the Electron Beam Irradiation Master Thesis Degree, Monash University, 2012.

[22] D.D. Khalyavin, A.N. Salak, N.P. Vyshatko, A.B. Lopes, N.M. Olekhnovich, A.V. Pushkarev, I.I. Maroz, Y.V. Radyush, Crystal structure of metastable perovskite Bi(Mg$_{1/2}$Ti$_{1/2}$)O$_3$: Bi-Based structural analogue of antiferroelectric PbZrO$_3$, Chem. Mater. 18 (2006) 5104–5110.

[23] A. Zeb, J.S. Ullah, F. Bamiduro, D. Hall, S.J. Milne, Temperature-stable dielectric ceramics based on Na$_{0.5}$Bi$_{0.5}$TiO$_3$, J. Eur. Ceram. Soc. 38 (2018) 1548–1555.